Supporting Information

Harnessing Synergistic Effects between Polymorphic Phase Boundary and Second-Phase Hardening for Enhanced Electromechanical Compatibility in KNN-Based Ceramics

Hongjiang Li [a], Ning Chen [b], Lipeng Fan [b], Yaozhen Yu [a], Shenyi Li [a], Yufei Du [a], Zhi Tan [b], Jie Xing [b], Xin Gu [a], Jianguo Zhu [b*], Xiang Liu [a*]

[a] Faculty of Material Science and Engineering, Kunming University of Science and Technology, Kunming, Yunnan, 650093, China

[b] College of Materials Science and Engineering, Sichuan University, Chengdu, Sichuan, 610064, China

E-mail address: nic0400@scu.edu.cn (Jianguo Zhu), lxjim@sina.com (Xiang Liu)

Supplementary notes

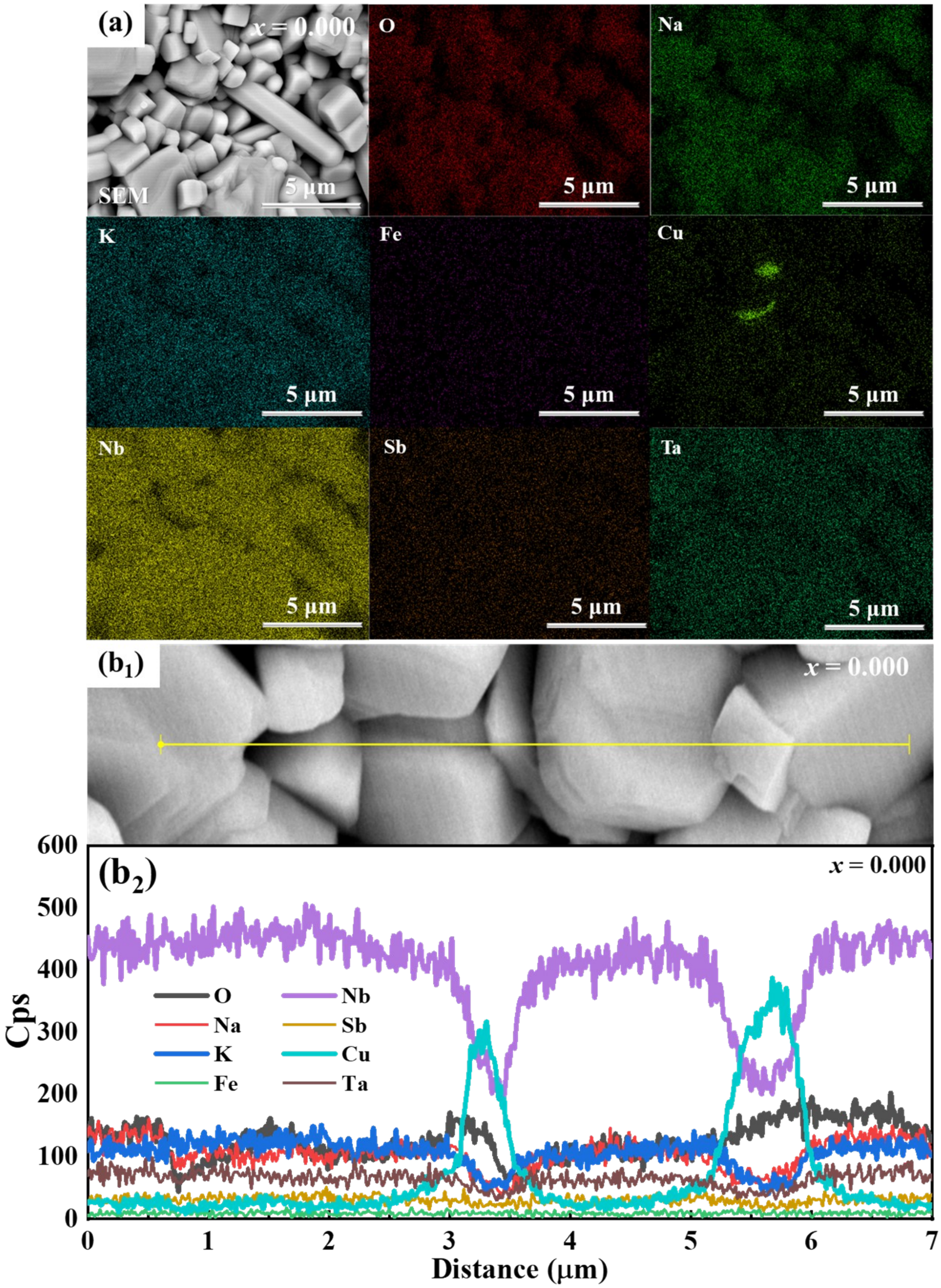

Fig. S1 (a) Backscattered electron SEM (BSE-SEM) image and corresponding elemental maps (O, Na, K, Fe, Cu, Nb, Sb, Ta) of the KNNT-0.000BNZ-BFO/CSO ceramic. (b$_1$) BSE-SEM image indicating the line-scan path (yellow). (b$_2$) Elemental line-scan profiles along the path shown in (b$_1$).

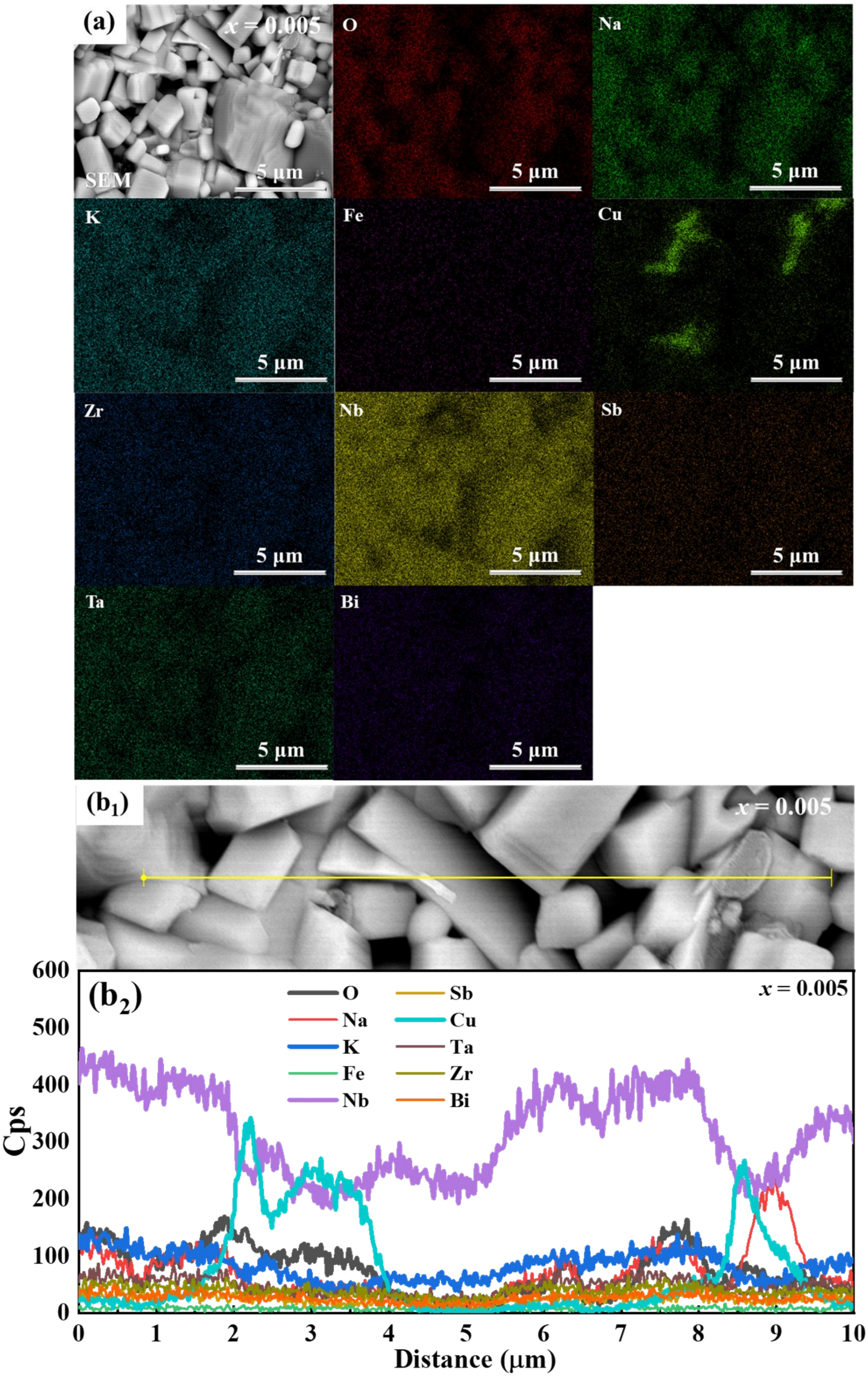

Fig. S2 (a) BSE-SEM image and corresponding elemental maps (O, Na, K, Fe, Cu, Zr, Nb, Sb, Ta, Bi) of the KNNT-0.005BNZ-BFO/CSO ceramic. (b$_1$) BSE-SEM image indicating the line-scan path (yellow). (b$_2$) Elemental line-scan profiles along the path shown in (b$_1$).

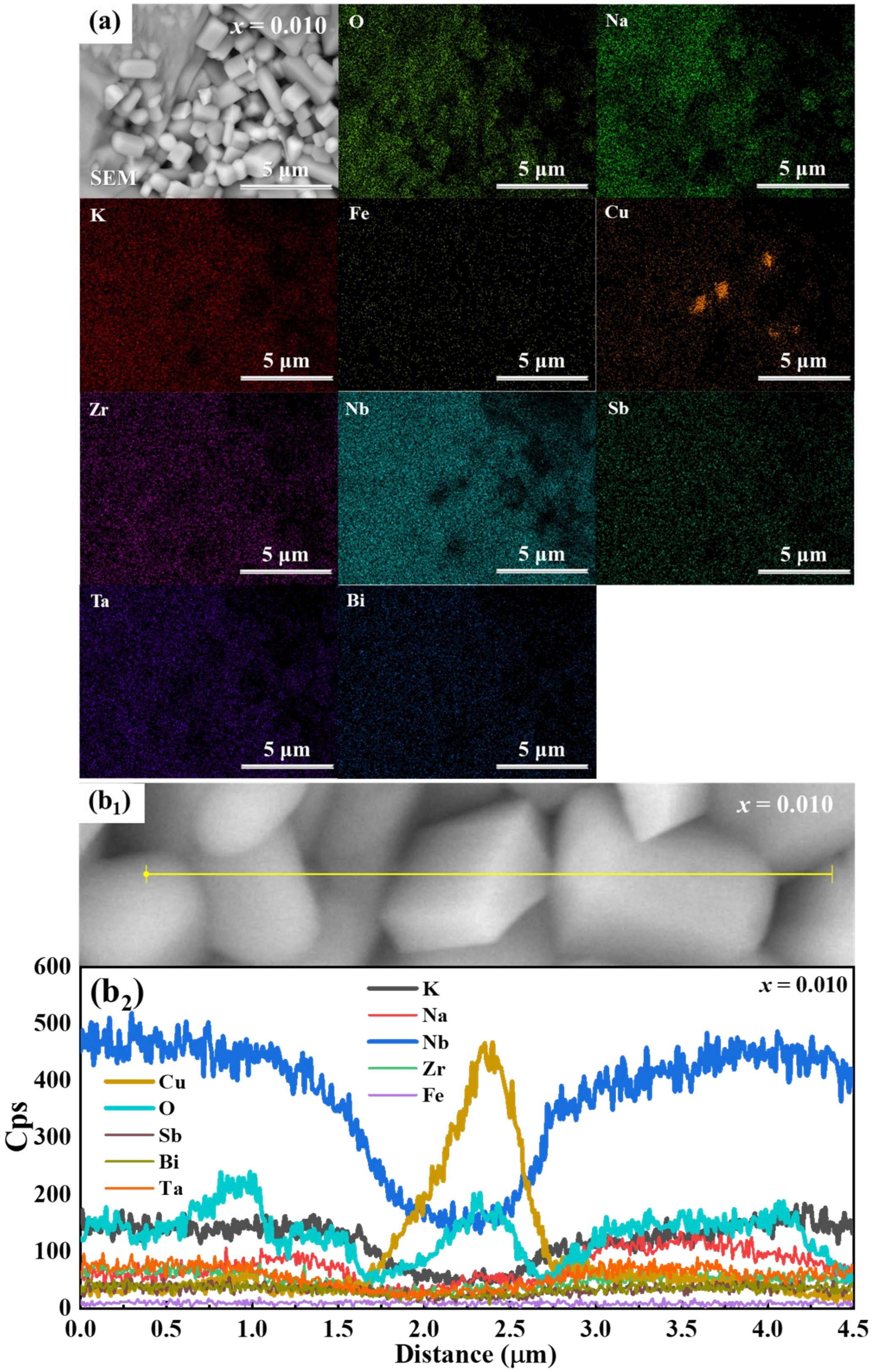

Fig. S3 (a) BSE-SEM image and corresponding elemental maps (O, Na, K, Fe, Cu, Zr, Nb, Sb, Ta, Bi) of the KNNT-0.010BNZ-BFO/CSO ceramic. (b_1) BSE-SEM image indicating the line-scan path (yellow). (b_2) Elemental line-scan profiles along the path shown in (b_1).

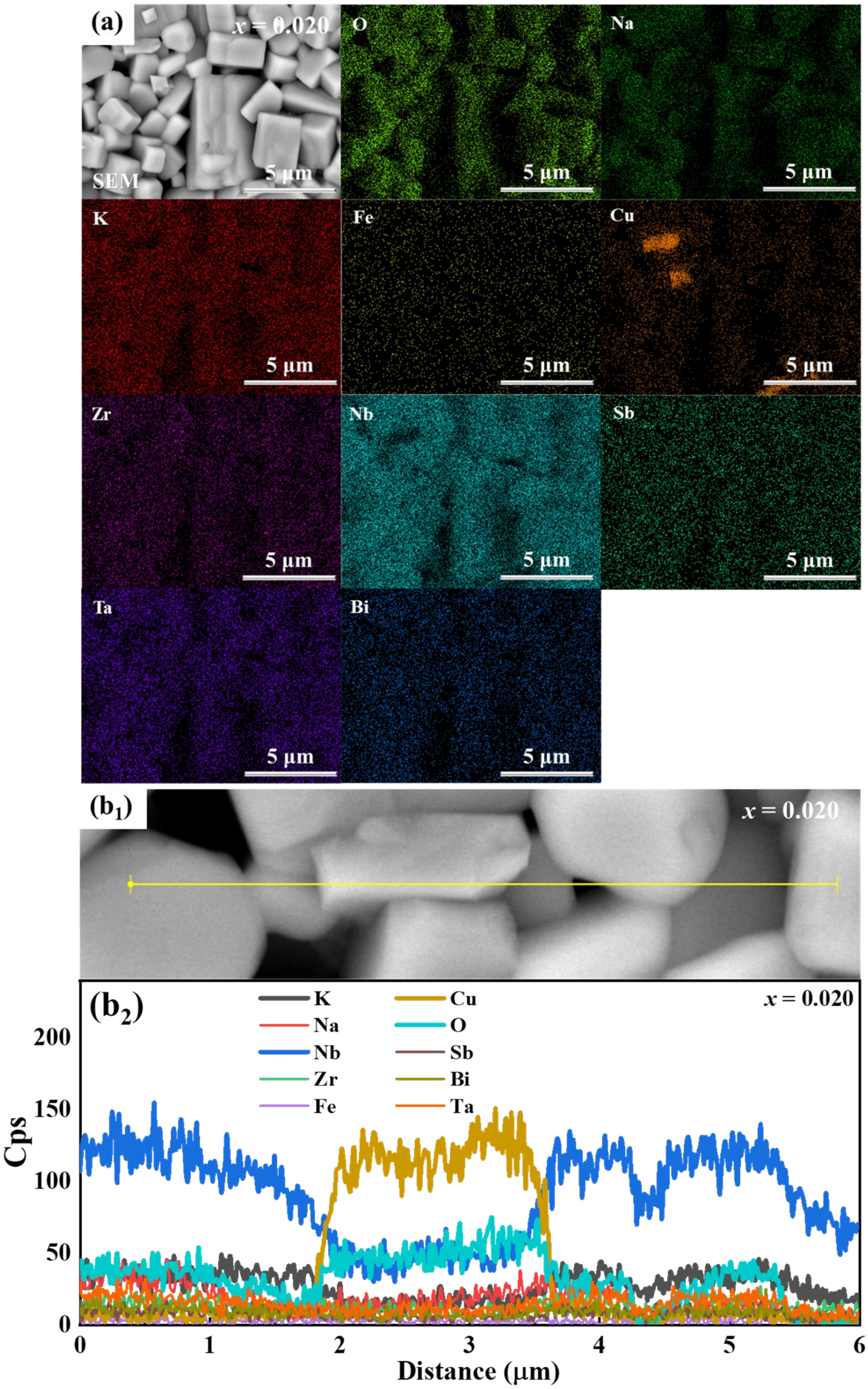

Fig. S4 (a) BSE-SEM image and corresponding elemental maps (O, Na, K, Fe, Cu, Zr, Nb, Sb, Ta, Bi) of the KNNT-0.020BNZ-BFO/CSO ceramic. (b_1) BSE-SEM image indicating the line-scan path (yellow). (b_2) Elemental line-scan profiles along the path shown in (b_1).

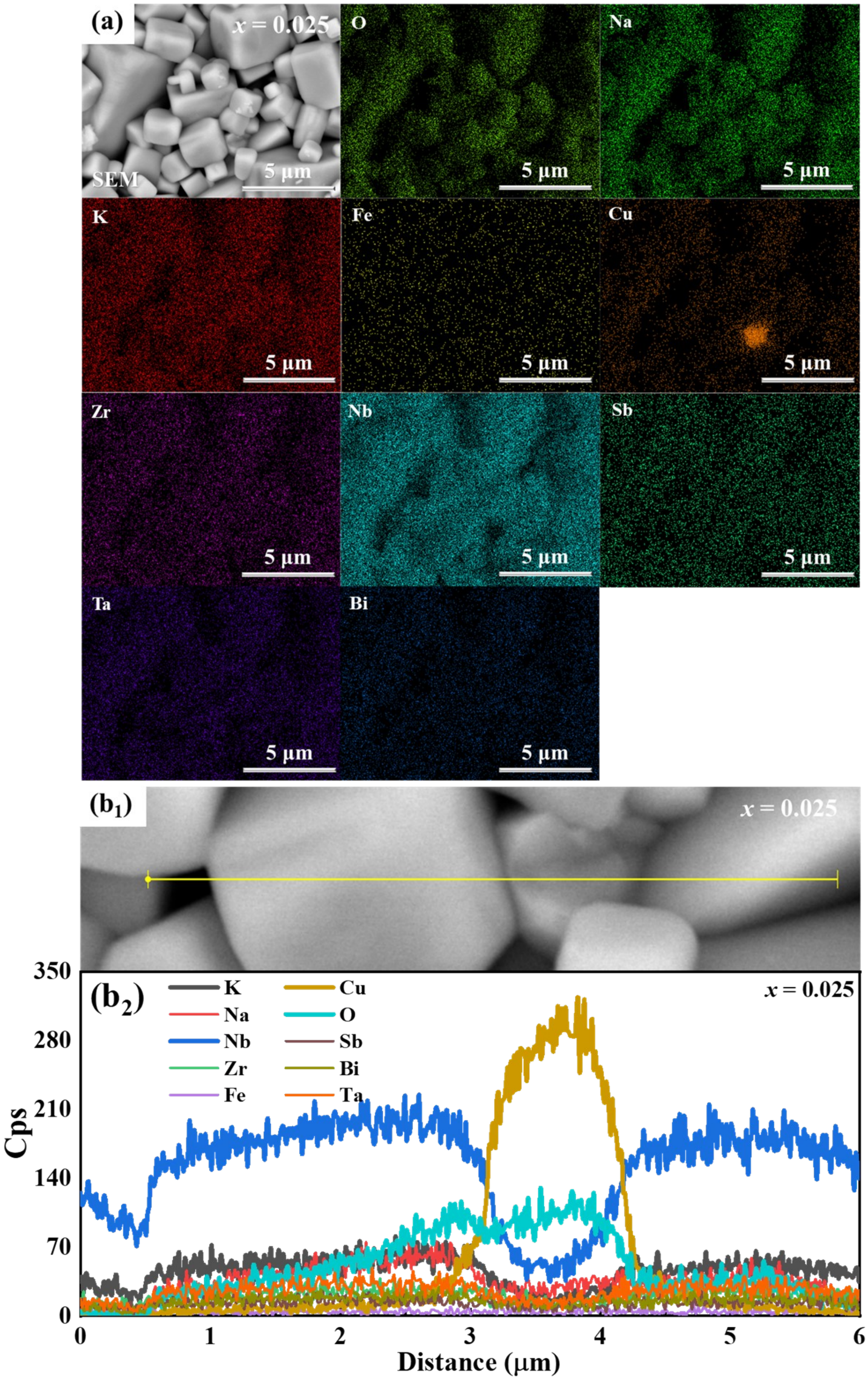

Fig. S5 (a) BSE-SEM image and corresponding elemental maps (O, Na, K, Fe, Cu, Zr, Nb, Sb, Ta, Bi) of the KNNT-0.025BNZ-BFO/CSO ceramic. (b_1) BSE-SEM image indicating the line-scan path (yellow). (b_2) Elemental line-scan profiles along the path shown in (b_1).

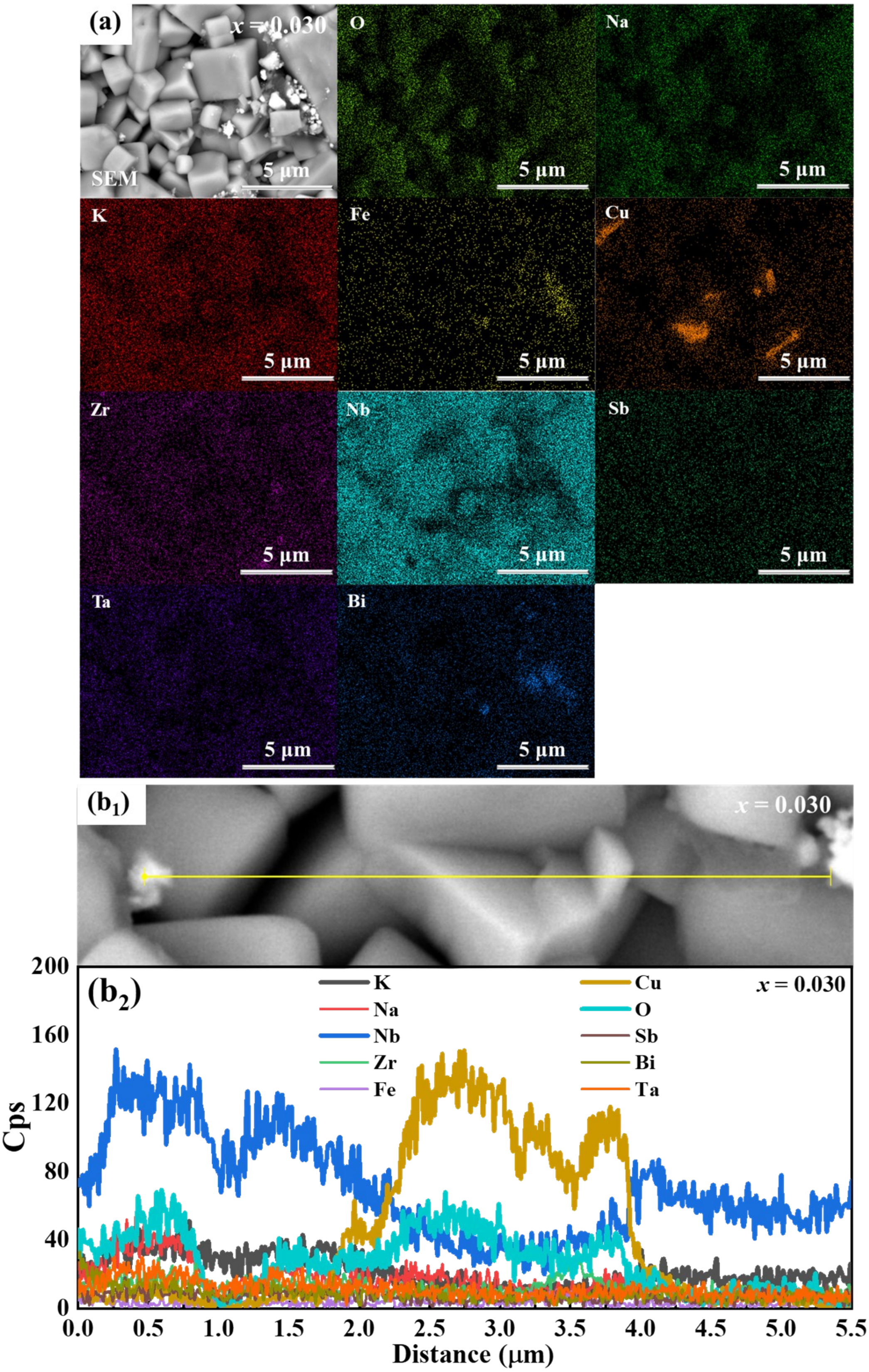

Fig. S6 (a) BSE-SEM image and corresponding elemental maps (O, Na, K, Fe, Cu, Zr, Nb, Sb, Ta, Bi) of the KNNT-0.030BNZ-BFO/CSO ceramic. (b_1) BSE-SEM image indicating the line-scan path (yellow). (b_2) Elemental line-scan profiles along the path shown in (b_1).

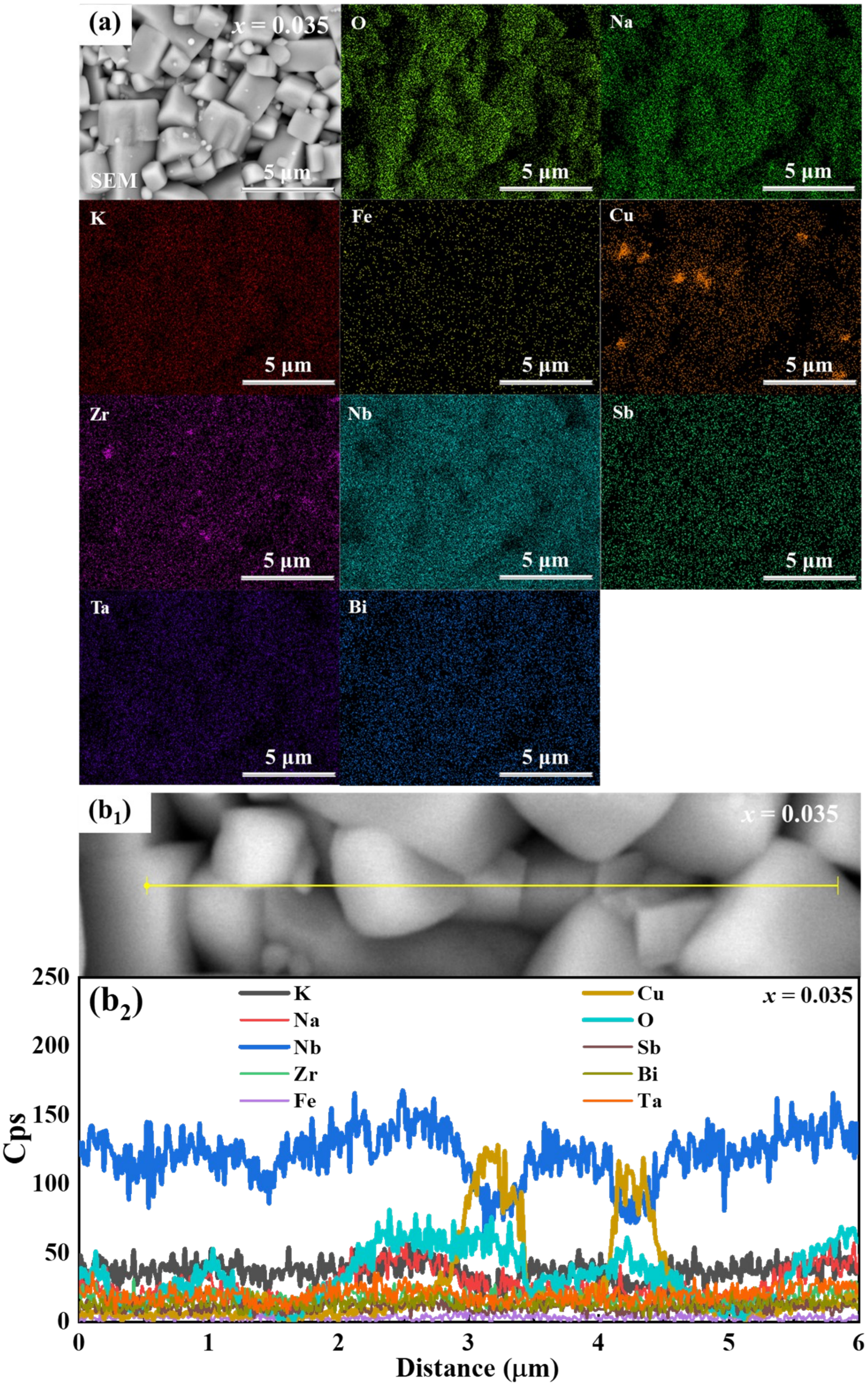

Fig. S7 (a) BSE-SEM image and corresponding elemental maps (O, Na, K, Fe, Cu, Zr, Nb, Sb, Ta, Bi) of the KNNT-0.035BNZ-BFO/CSO ceramic. (b$_1$) BSE-SEM image indicating the line-scan path (yellow). (b$_2$) Elemental line-scan profiles along the path shown in (b$_1$).

The BSE-SEM images of the KNNT-xBNZ-BFO/CSO ceramics are shown in Fig. S8. The average grain size (AGS) of ceramics shows a trend of first decreasing, then increasing, and then decreasing as x increases from 0.000 to 0.035. The non-monotonic variation of AGS with increasing x value is primarily influenced by phase transformations and their associated defect chemistry. Initially, at low x values (orthorhombic-tetragonal (O-T) phase), the reduction in grain size may be attributed to increased tetragonal phase content. Within tetragonal symmetry, greater tetragonal distortion is anticipated due to the presence of internal lattice stresses, which exert a more detrimental effect on grain growth. As x increases, the transition to the rhombohedral-orthorhombic-tetragonal (R-O-T) phase reduces internal strain and promotes grain coalescence due to enhanced ion diffusion facilitated by oxygen vacancies. At higher x values (R-T phase), increased tetragonal content also inhibits grain growth. The suppressed grain growth can be ascribed to the hindered mass transportation during the sintering process caused by over-doping. Thanks to the intrinsic disordered lattice distortion arising from the disordered composition distribution. Intrinsic disordered lattice distortion leads to sluggish diffusion and fine grains[1].

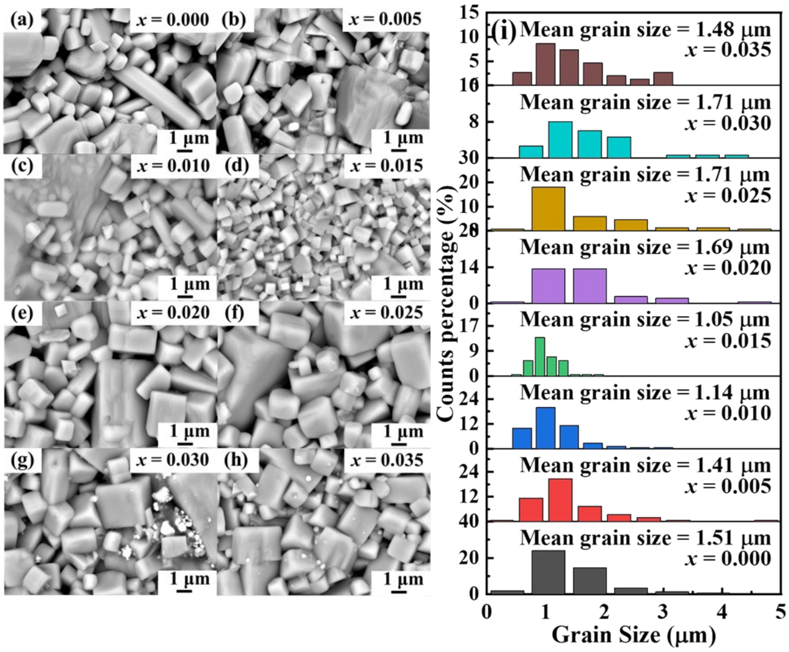

Fig. S8 (a-h) BSE-SEM images of KNNT-xBNZ-BFO/CSO ceramics with varying BNZ content. (i) Grain size distribution and the corresponding AGS for each composition.

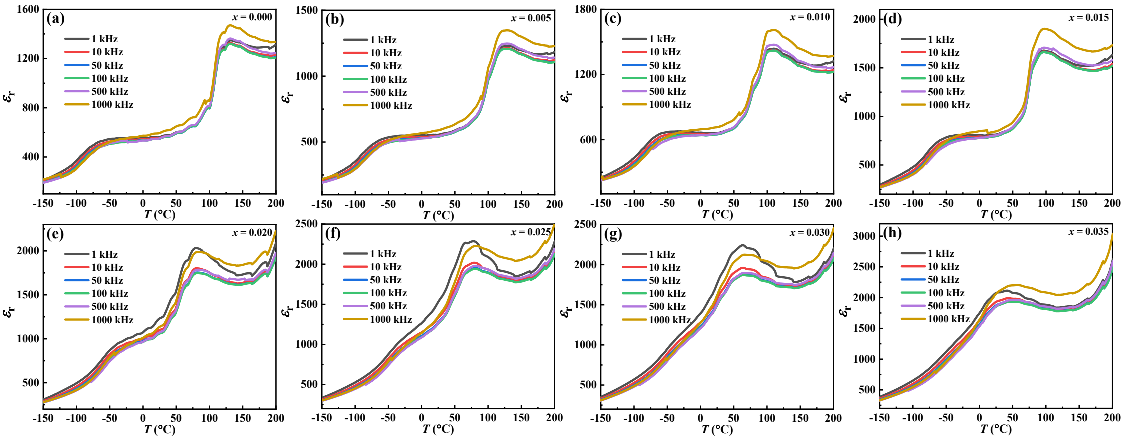

Fig. S9 (a-h) Temperature-dependent relative permittivity (ε_r) of KNNT-*x*BNZ-BFO/CSO ceramics measured from -150 to 200 °C.

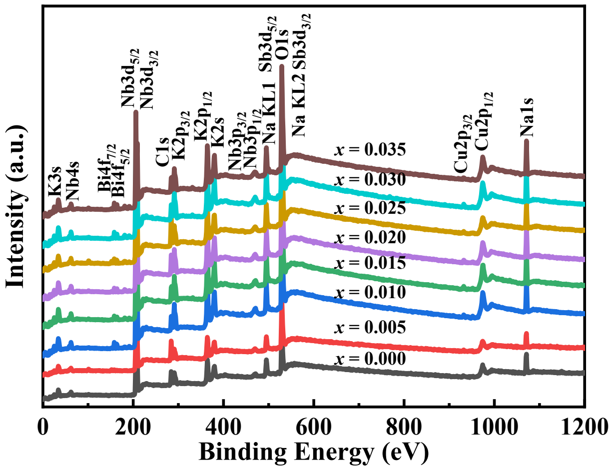

Fig. S10 X-ray photoelectron spectroscopy (XPS) spectra of the KNNT-*x*BNZ-BFO/CSO ceramics.

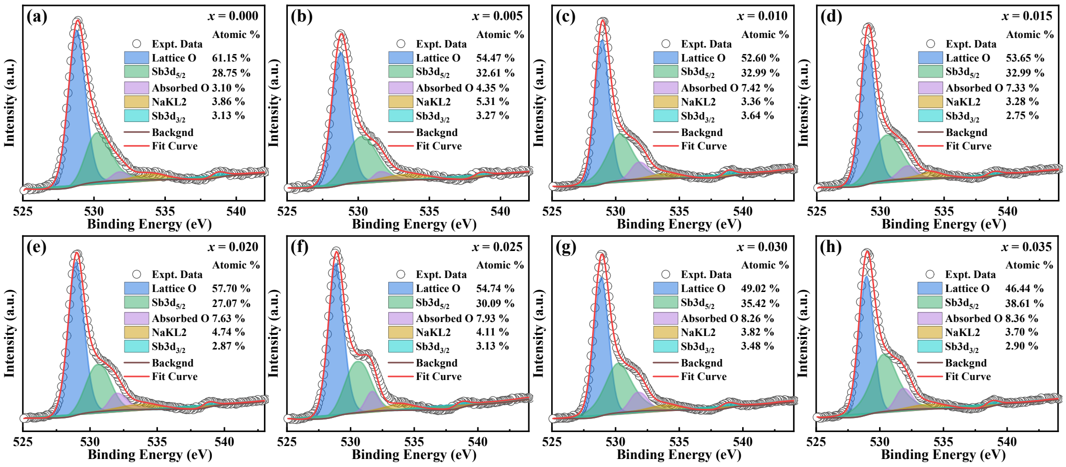

Fig. S11 High-resolution XPS spectra and corresponding peak fitting for the O 1s, Sb 3d, and Na KL2 regions of KNNT-xBNZ-BFO/CSO ceramics.

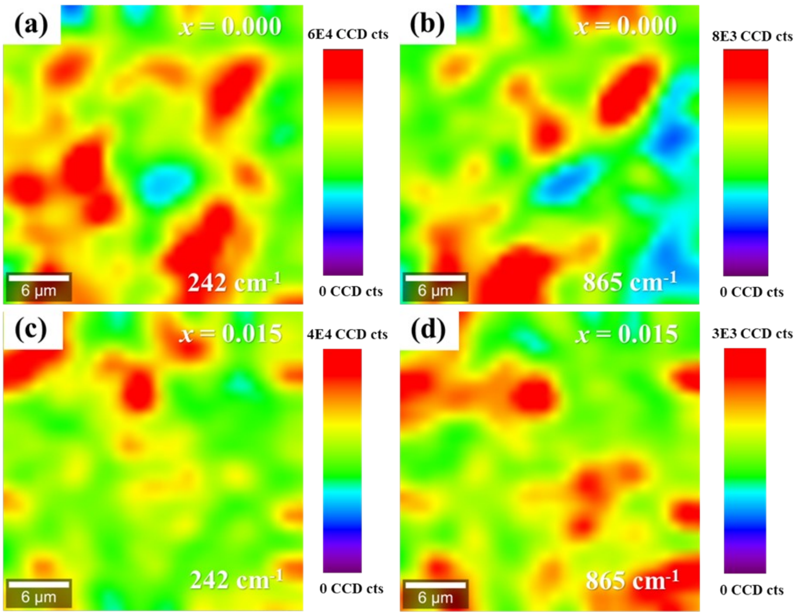

Fig. S12 Raman mapping results are output with the characteristic peak area as a parameter and presented in a color scheme, wearing brighter colors in the plot represent larger peak areas and vice versa. The peak area of (a) the characteristic peak 242 cm^{-1} and (b) the characteristic peak 865 cm^{-1} of KNNT-0.000BNZ-BFO/CSO ceramic is used as a parameter to output Raman mapping results. The peak area of (c) the characteristic peak 242 cm^{-1} and (d) the characteristic peak 865 cm^{-1} of KNNT-0.015BNZ-BFO/CSO ceramic is used as a parameter to output Raman mapping results.

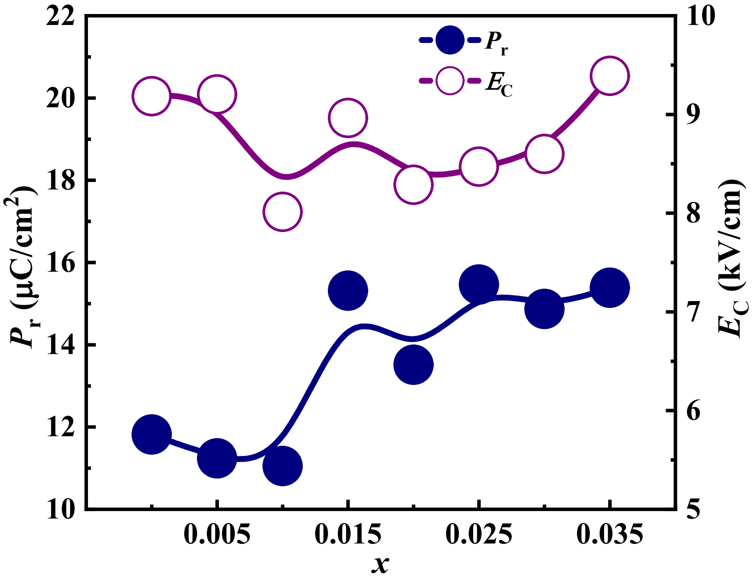

Fig. S13 The changes of P_r and E_C for the KNNT-*x*BNZ-BFO/CSO ceramics with the addition of BNZ content.

The intrinsic and extrinsic contributions to piezoelectricity can be quantitatively distinguished within the sub-coercive electric field region using the Rayleigh analysis[2-4]. The intrinsic contribution is primarily governed by the crystal lattice deformation, whereas the extrinsic contribution arises mainly from domain wall motion. For piezoelectric materials, this relationship is described by the following equations[5]:

$$P(E_0) = (\varepsilon_{\mathrm{init}} + \alpha E_0)E_0 \tag{1}$$

$$P(E) = (\varepsilon_{\mathrm{init}} + \alpha E_0)E_0 \pm (E_0^2 - E^2)/2 \tag{2}$$

$$\varepsilon^{*}(E_0) = \varepsilon_{\mathrm{init}} + \alpha E_0 \tag{3}$$

where $P(E)$ denotes the polarization, ε^{*} referred to as the field-dependent (Rayleigh) dielectric permittivity, and E_0 is the amplitude of the applied electric field. To avoid the nucleation of new domains, E_0 is maintained below one-third of the E_C. The parameter $\varepsilon_{\mathrm{init}}$ described as the reversible, field-independent component of the dielectric permittivity[6], corresponding to the material's polarization capability under nearly loss-free conditions. It originates from the combined effects of the intrinsic lattice response and the reversible motion of internal interfaces, comprising both the intrinsic and reversible extrinsic contributions. In contrast, the coefficient α quantifies the irreversible piezoelectric response arising from domain wall motion[2]. αE_0 is attributed to the irreversible extrinsic contribution, which is the core source of dielectric nonlinearity and loss. Fig. S14a-h shows the typical P-E_0 curves for the KNNT-xBNZ-BFO/CSO ceramics. Based on Rayleigh measurements, the ε^{*} is calculated from the difference between positive and negative polarization ($P_{\mathrm{p\text{-}p}}$) values at each electric field amplitude E_0 as follows:

$$\varepsilon^{*} = P\mathrm{p}\square\mathrm{p}/2E_0 \tag{4}$$

The linearity of ε^{*}-E_0 confirms the applicability of the Rayleigh approach in the chosen field region, as shown in Fig. S14i. The Rayleigh coefficient of $\varepsilon_{\mathrm{init}}$ and α can be calculated by fitting the linear ε^{*} - $E0$ plots with equation (3). Rayleigh analysis reveals that the $\varepsilon_{\text{init}}$ increases gradually with BNZ content, while the α first rises and then declines (Fig. S14l). Specifically, $\varepsilon_{\text{init}}$ peaks at the R-T phase boundary, whereas α reaches its maximum at the R-O-T phase boundary. In the R-O-T triple-phase region, the coexistence of <111> (R), <011> (O), and <001> (T) polarizations promotes a high density of diverse non-180° domain walls. These walls are weakly pinned and easily undergo irreversible motion under low electric fields, leading to the observed maximum in α. In contrast, the R-T phase boundary exhibits a flatter free-energy landscape, significantly reducing the energy barrier for polarization rotation between R and T variants. This enhances intrinsic lattice response and facilitates reversible domain wall vibrations, shifting the contribution of certain domain dynamics from irreversible (α) to reversible ($\varepsilon_{\text{init}}$). As a result, the synergy between low barrier polarization rotation and enhanced reversible domain activity drives $\varepsilon_{\text{init}}$ to its peak at the R-T boundary. The proportion of the irreversible extrinsic contribution to the total dielectric response, expressed as $\alpha E_0/(\varepsilon_{\text{init}} + \alpha E_0)$[7], gradually decreases for $x \leq 0.02$ and fluctuates between 0.02 and 0.035 (Fig. S14m). The initial decrease is primarily attributed to the increasing proportion of the T phase within the O-T phase boundary, which enhances the intrinsic lattice response. This enhancement arises because lattice deformation induces internal ionic rearrangements that minimize the system's free energy. Specifically, the intrinsic lattice response originates from field-induced ionic displacements within the unit cell. In non-centrosymmetric phases (e.g., the T phase), such displacements along specific polar axes efficiently lower the system's Gibbs free energy, leading to a pronounced strain response. In the R phase structure, Nb atoms can rearrange by stretching or contracting the Nb-O bond, resulting in a small displacement change. In contrast, the O and T phases possess one and two directions, respectively, capable of generating large polarization changes, which accounts for the generally higher piezoelectricity of the T phase compared to the O and R phases. The fluctuation observed at $x = 0.025$ is likely due to the R-O-T phase coexistence, which provides a greater irreversible extrinsic contribution than the O-T or R-T phase coexistence.

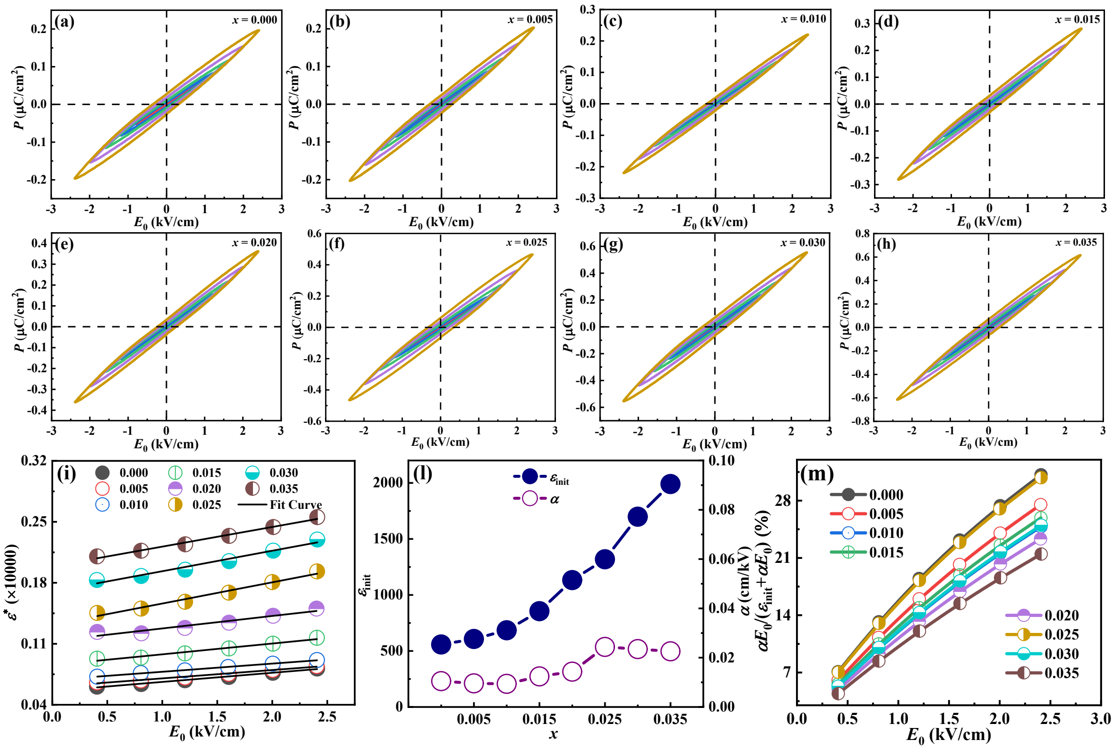

Fig. S14 (a-h) Typical *P*-*E* curves in the sub-coercive electric field region for the KNNT-*x*BNZ-BFO/CSO ceramics. (i) ε^* value as a function of E_0. (l) Composition-dependent variations of the α and $\varepsilon_{\text{init}}$ Rayleigh parameters. (m) $\alpha E_0/(\varepsilon_{\text{init}} + \alpha E_0)$ value as a function of E_0.

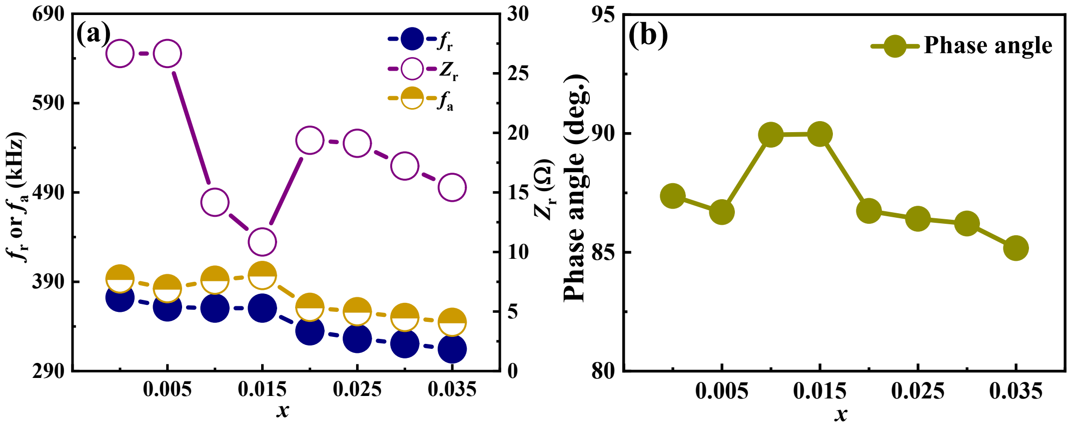

Fig. S15 The changes of (a) f_r, f_a, Z_r, and (b) phase angle for the KNNT-*x*BNZ-BFO/CSO ceramics with the addition of BNZ content.

The temperature-dependent dielectric properties of the KNNT-*x*BNZ-BFO/CSO ceramics are analyzed using a modified Curie-Weiss law[8-10], as shown in Fig. S16 and

Fig. S17. The diffuse-phase transition behavior of perovskite ferroelectrics can be expressed using this law, which relates the dielectric constant (ε) to temperature (T) and a constant (C). The modified Curie-Weiss law is shown in Equation 5.

$$\varepsilon = \frac{C}{(T - T0)} \tag{5}$$

$$\Delta T_m = T_{cw} - T_m \tag{6}$$

$$1/\varepsilon_r - 1/\varepsilon_m = \frac{(T - T_m)^\gamma}{C} \tag{7}$$

The change in diffuse phase transition behavior of the ceramics is evaluated using the values of ΔT_m and diffuseness index (γ)[11]. ΔT_m is the difference between the transition temperature (T_m) and the Curie-Weiss temperature (T_{cw}), as shown in Equation 6. The γ is calculated using Equation 7, which relates the dielectric constants at the maximum (ε_m) and the transition (ε_r) temperatures to the temperature and the constant (C). Fig. S17 shows the $\log(1/\varepsilon_r - 1/\varepsilon_m)$ as a function of $\log(T-T_m)$ curves, which can be used to evaluate the diffuseness of the ceramics. Generally, it is well known that the relaxor behavior in ferroelectrics is induced by polar nanoregions (PNRs), leading to a phase instability[12, 13]. The diffuseness factor is used to describe the degree of relaxor: $\gamma = 1$ for normal ferroelectrics without PNRs, and $\gamma = 2$ for ideal relaxor ferroelectrics without long-range ferroelectric domains.

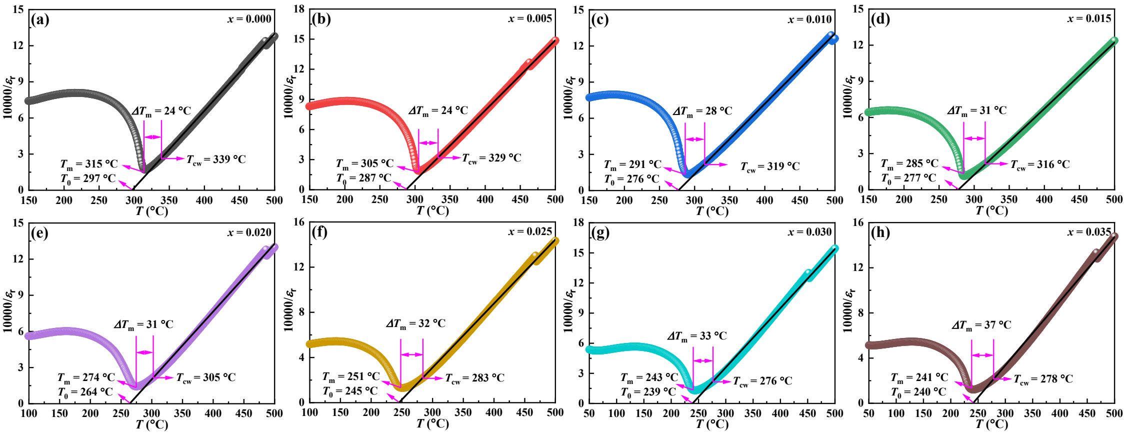

Fig. S16 (a-h) The relationship between the temperature and inverse dielectric permittivity of the KNNT-xBNZ-BFO/CSO ceramics.

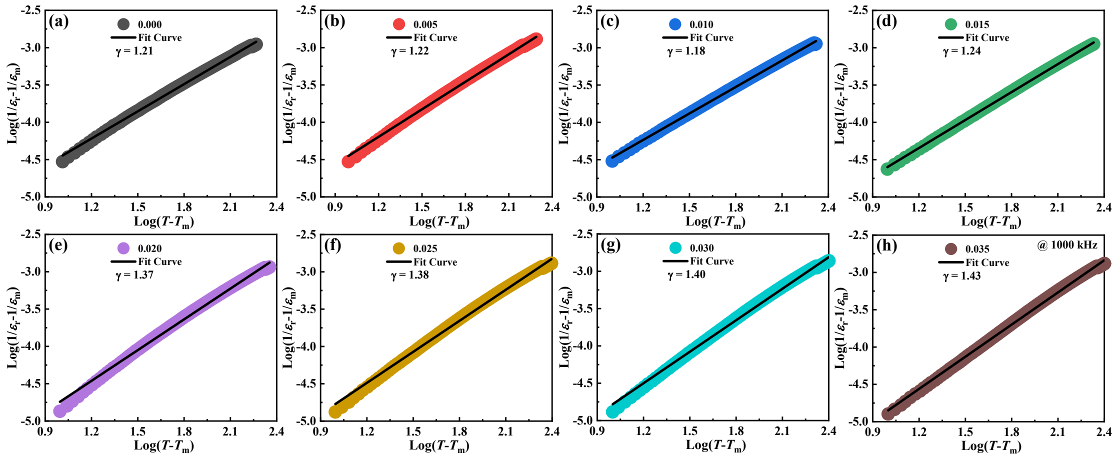

Fig. S17 (a-h) A plot of log($1/\varepsilon_r$-$1/\varepsilon_m$) as a function of log(T-T_m) for the KNNT-*x*BNZ-BFO/CSO ceramics.

Table S1 Comparison of the comprehensive properties between the KNNT-0.015BNZ-BFO/CSO ceramic and other reported KNN-based systems.

Material System/ Preparation technology	d_{33} (pC/N)	Q_m	k_p
KNNT-BNZ-0.2MnO_2[14]	330	135	0.388
KNN-BNH-Cu-0.25Fe[15]	340	211	0.46
T1-MnKNN[16]	370	150	0.51
GBD technique[17]	360	132	~0.45
KNLNST+KCT+Ni_2O_3[18]	287	~180	0.462
2KNCN/N_2[19]	158	206	0.417
KNN-BKT+0.8MnO[20]	221	143	0.447
LNKN[21]	229	220	0.40
NKN-BTS[22]	256	111	0.42
KNN-BaSn[23]	257	123.4	0.405
0.95KNN-0.05LNS-0.8% CuO[24]	207	320	0.44
LT-KNN+1mol% CuO[25]	185	323	0.37
0.93NKN-0.07LN+1.5mol% CuO[26]	170	560	0.37
KNN-Cu-0.5Co[27]	83	577	0.3
KNN-*x*BNZ-1%CuO-0.2%Fe_2O_3[28]	231	355	0.44
KNNT-BNZ-0.01Cu[29]	260	210	0.45
KNNT+1 mol% KCN[30]	89	818	0.401
This work	240	500	0.51

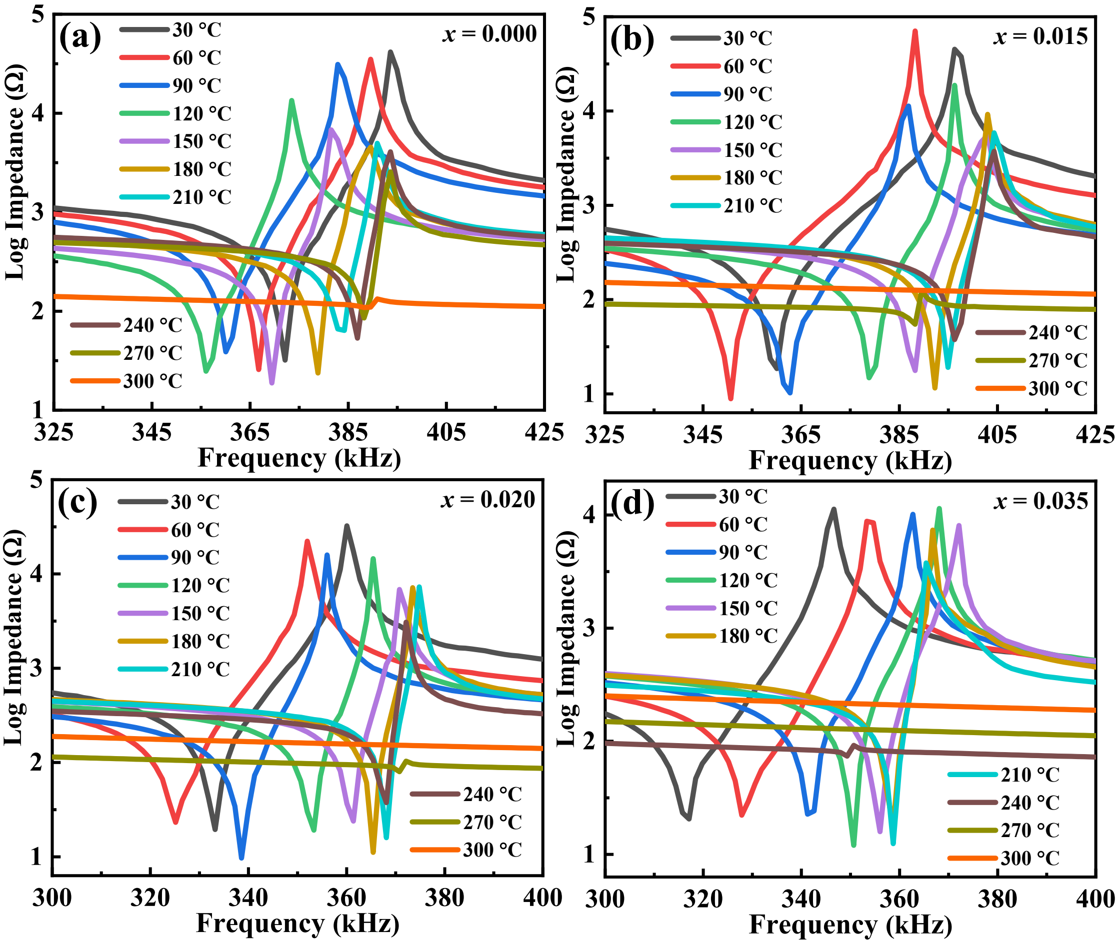

Fig. S18 *In-situ* temperature dependence of the first radial mode frequency shift of the KNNT-*x*BNZ-BFO/CSO ceramics measured from 30 to 300 °C: (a) $x = 0.000$, (b) $x = 0.015$, (c) $x = 0.020$, and (d) $x = 0.035$.

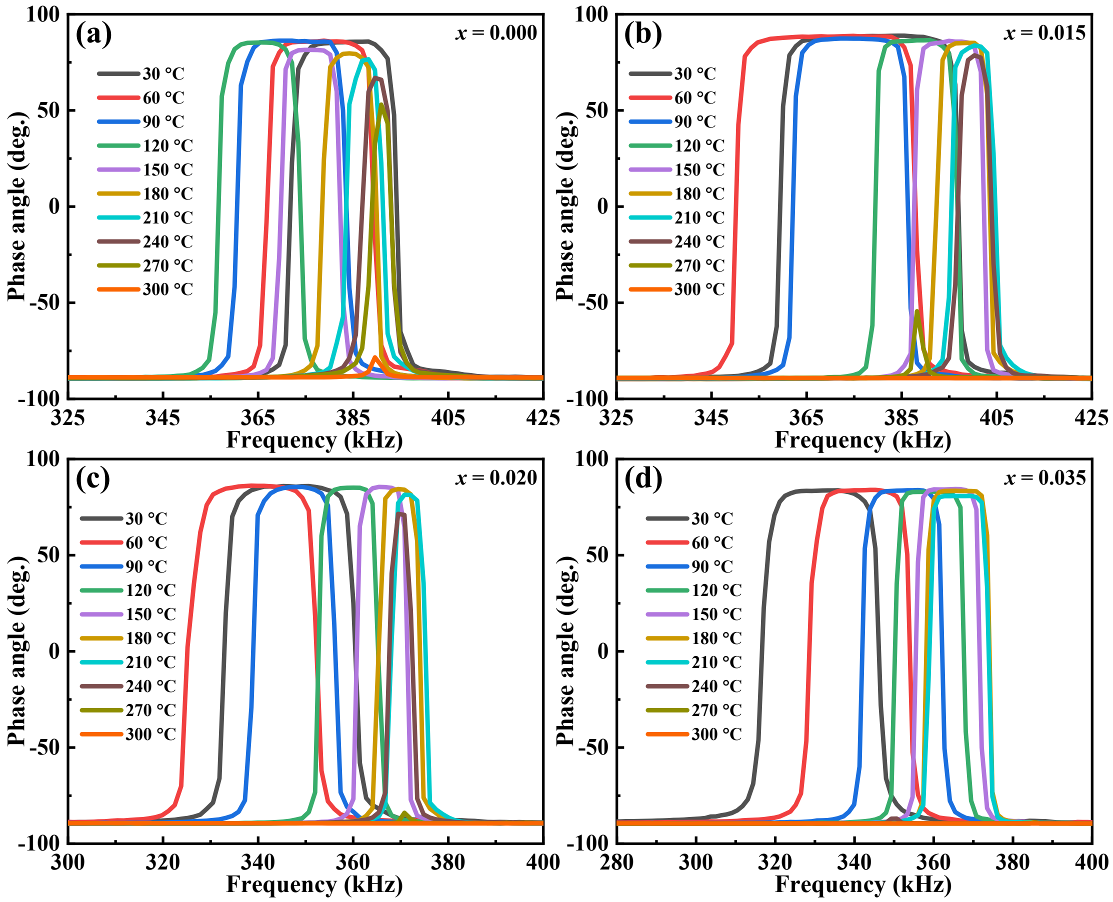

Fig. S19 *In-situ* temperature dependence of the phase angle of the KNNT-*x*BNZ-BFO/CSO ceramics measured from 30 to 300 °C: (a) *x* = 0.000, (b) *x* = 0.015, (c) *x* = 0.020, and (d) *x* = 0.035.

References

1. Y. Zhang, L. Chen, H. Liu, S. Deng, H. Qi and J. Chen, *InfoMat*, 2023, 5, e12488.
2. Y. Liu, Q. Li, L. Qiao, Z. Xu and F. Li, *Advanced Science*, 2022, 9, 2204631.
3. P. Wang, Q. Guo, F. Li, F. Xia, H. Hao, H. Sun, H. Liu and S. Zhang, *Journal of the American Ceramic Society*, 2021, 104, 5127-5137.
4. H. Zhao, Y. Hou, X. Yu, M. Zheng and M. Zhu, *Acta Materialia*, 2019, 181, 238-248.
5. D. Damjanovic and M. Demartin, *Journal of Physics D: Applied Physics A*, 1996, 29, 2057-2060.
6. S. Pal, A. B. Swain, P. P. Biswas and P. Murugavel, *Physical Review Materials*, 2020, 4, 064415.
7. M. Abebe, K. Brajesh and R. Ranjan, *Journal of Applied Physics*, 2017, 122, 034101.
8. J. Xing, S. Xie, B. Wu, Z. Tan, L. Jiang, L. Xie, Y. Cheng, J. Wu, D. Xiao and J. Zhu, *Scripta Materialia*, 2020, 177, 186-191.
9. J. Xing, Z. Tan, L. Xie, L. Jiang, J. Yuan, Q. Chen, J. Wu, W. Zhang, D. Xiao and J. Zhu, *Journal of the American Ceramic Society*, 2018, 101, 1632-1645.
10. M.-H. Zhang, Q. Zhang, T.-T. Yu, G. Li, H.-C. Thong, L.-Y. Peng, L. Liu, J. Ma, Y. Shen, Z. Shen, J. Daniels, L. Gu, B. Han, L.-Q. Chen, J.-F. Li, F. Li and K. Wang, *Materials Today*, 2021, 46, 44-53.
11. X. Ren, Z. Peng, B. Chen, Q. Shi, X. Qiao, D. Wu, G. Li, L. Jin, Z. Yang and X. Chao,

Journal of the European Ceramic Society, 2020, 40, 2331-2337.

12. F. Li, S. Zhang, D. Damjanovic, L.-Q. Chen and T. R. Shrout, *Advanced Functional Materials*, 2018, 28, 1801540.
13. G. Xu, J. Wen, C. Stock and P. M. Gehring, *Nature Materials*, 2008, 7, 562-566.
14. W. Luo and Z. Shen, *Ceramics-Silikaty*, 2019, 63, 399-402.
15. Y. Cheng, S. Guan, Q. Wang, X. Wu, J. Xing, L. Jiang, Z. Tan and J. Zhu, *Journal of the European Ceramic Society*, 2024, 44, 6978-6986.
16. Y. Guan, Y. Sun, J. Wang, G. Huangfu, H. Li, S. Zhang and Y. Guo, *ACS Applied Materials & Interfaces*, 2023, 15, 51421-51428.
17. Y. Zhang, X. Feng, F. Li, D. Meng, T. Zheng and J. Wu, *Advanced Functional Materials*, 2023, 33, 2306039.
18. Q. Zhang, F. Xu, R. Yang, Y. Lu, P. Li, X. Shang, T. Zhou and Y. He, *Ceramics International*, 2017, 43, 2537-2540.
19. X. Qi, P. Ren and X. Tong, *Ceramics International*, 2023, 49, 34795-34804.
20. X. P. Jiang, Y. Chen, K. H. Lam, S. H. Choy and J. Wang, *Journal of Alloys and Compounds*, 2010, 506, 323-326.
21. H. Li, B. Zhang, Q. Li and R. Xu, *Advanced Materials Research*, 2011, 415-417, 1679-1682.
22. Y.-J. Cha, Y. H. Jeong, Y.-J. Lee, J.-H. Paik and S. Nahm, *Japanese Journal of Applied Physics*, 2010, 49, 020205.
23. Z. Yang, Y. Fan, Y. Jia, X. Chen, K. Shang, S. Tang, H. Fan and W. Wang, *Ceramics International*, 2024, 50, 42237-42246.
24. Y. Zhao, Y. Zhao, R. Huang, R. Liu and H. Zhou, *Journal of the American Ceramic Society*, 2011, 94, 656-659.
25. Z.-Y. Shen, Y. Xu and J.-F. Li, *Ceramics International*, 2012, 38S, S331-S334.
26. M.-K. Choi, H.-Y. Park, I.-T. Seo, J.-H. Choi, W. Kim, S. Nahm and H.-J. Lee, *Current Applied Physics*, 2011, 11, 598-603.
27. W. Wu, M. Chen, J. Li, Y. Ding and C. Liu, *Journal of Alloys and Compounds*, 2016, 670, 128-134.
28. Y. Xie, J. Xing, Z. Tan, L. Xie, Y. Cheng, X. Wu, R. Han, Q. Chen and J. Zhu, *Ceramics International*, 2022, 48, 6565-6573.
29. Y. Cheng, W. Fan, H. Chen, L. Xie, J. Xing, Z. Tan and J. Zhu, *ACS Applied Materials & Interfaces*, 2022, 14, 55803-55811.
30. Y. G. Lv, C. L. Wang, J. L. Zhang, M. L. Zhao, M. K. Li and H. C. Wang, *Materials Letters*, 2008, 62, 3425-3427.